Inorganic Chemistry
Article
pubs.acs.org/IC

Upconversion Effective Enhancement by Producing Various Coordination Surroundings of Rare-Earth Ions

Qingming Huang,[†,‡] Han Yu,[†] En Ma,[§] Xinqi Zhang,[‡] Wenbing Cao,[†] Chengang Yang,[†] and Jianchang Yu*[,†]

[†]College of Materials Science and Engineering, Fuzhou University, Fuzhou, Fujian 350108, China
[‡]Instrumentation Analysis and Research Center, Fuzhou University, Fuzhou, Fujian 350002, China
[§]Fujian Institute of Research on the Structure of Matter, Chinese Academy of Sciences, Fuzhou, Fujian 350002, China

S *Supporting Information*

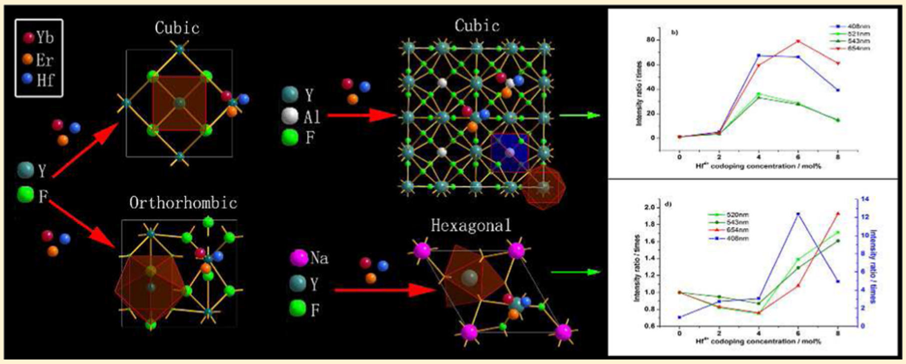

ABSTRACT: In this manuscript, we present a simple route to enhance upconversion (UC) emission by producing two different coordination sites of trivalent cations in a matrix material and adjusting crystal field asymmetry by Hf^{4+} co-doping. A cubic phase, $Y_{3.2}Al_{0.32}Yb_{0.4}Er_{0.08}F_{12}$, with these structural characteristics was synthesized successfully by introducing a small ion (Al^{3+}) into YF_3. X-ray diffraction (XRD), nuclear magnetic resonance (NMR), transmission electron microscopy (TEM), X-ray spectroscopy (XPS), and fluorescence spectrophotometry (FS) were employed for its crystalline structure and luminescent property analysis. As a result, the coordination environments of the rare-earth ions were varied more obviously than a hexagonal $NaYF_4$ matrix with the same Hf^{4+} co-doping concentration, with vertical comparison, UC luminescent intensities of cubic $Y_{3.2}Al_{0.32}Yb_{0.4}Er_{0.08}F_{12}$ were largely enhanced (~32−80 times greater than that of different band emissions), while the maximum enhancement of hexagonal $NaYF_4$ was by a factor of ~12. According to our experimental results, the mechanism has been demonstrated involving the crystalline structure, crystal field asymmetry, luminescence lifetime, hypersensitive transition, and so on. The study may be helpful for the design and fabrication of high-performance UC materials.

1. INTRODUCTION

Recently, anti-Stokes emission nanocrystals have converted infrared (IR) radiation to visible luminescence,[1,2] which are promising for applications in biomedical imaging,[3,4] drug delivery,[5,6] photodynamic therapy,[7,8] solar energy conversion,[9,10] and temperature sensors.[11,12] All of them are highly dependent on the upconversion (UC) luminescent properties. Urged by the potential applications, enormous endeavors have been made to improve the UC performance, such as sensitizer co-doping,[13,14] core−shell structure design,[15,16] metal plasma resonance,[17,18] surface modification,[19] high excitation irradiance,[20] constructing nanoantenna architecture,[21] choice of sublattice energy cluster crystal structure matrix,[22] and different radius or valence ion co-doping.[23,24] However, none of these methods, except constructing nanoantenna architecture, have achieved the desired results for complex material preparation or the limited improvement of luminescence efficiency. The complex nanoantenna architecture was only fitting for solar energy application and cannot be applied in biomedical imaging or photodynamic therapy for the large complex device frame, and the high-density excitation method requires expensive laser equipment and is harmful for *in vivo* cells. There, exploration of a new method to improve UC efficiency remains a worthy project. According to Judd−Ofelt theory[25,26] and our team's previous investigation,[27,28] UC efficiency can be enhanced by tuning crystal field asymmetry. In our previous investigation, $Er^{3+}/Yb^{3+}/Y^{3+}$ ions were located in two sites of hexagonal $NaYF_4$ as the matrix with the same ligancy to F^-. When the matrix was co-doped with Sc^{3+} or $Sn^{2+/4+}$, the crystal field asymmetry was tuned in a small scale, since the diversity of the rare-earth ion surroundings was not obvious. For this reason, we conceive of synthesizing a matrix with two or more Wyckoff positions and with different coordination numbers of Er^{3+}/

Received: November 21, 2014
Published: February 27, 2015

DOI: 10.1021/ic5027976
Inorg. Chem. 2015, 54, 2643−2651

Yb^{3+}/Y^{3+} to F^-. When an ion with different radius or valence is co-doped into this matrix, the crystal field asymmetry may be tuned largely and the coordination environment of rare-earth ions may become varied. As a result, the electronic super-sensitive transition will be improved and the UC luminescence quenching will be inhibited,[29] leading to higher UC efficiency.

To verify our theory, three smaller various ions (Al^{3+}, Ga^{3+}, or In^{3+}) were introduced to F^- and $Y^{3+}/Er^{3+}/Yb^{3+}$ reaction system, respectively. Moreover, Hf^{4+}, as a dopant, was induced into an anchored reaction system to tune the crystalline lattice structure. The schematic diagram is shown in Figure 1, which shows that, when rare-earth ions Yb^{3+} and Er^{3+} were added in the F^- or Y^{3+} ion reaction system, its structure would become cubic or orthorhombic. While a smaller-radius ion M (Al, Ga, In) was added in the reaction system synchronously, it would become a cubic phase with two different coordination environments of the trivalent cations. If further tridoped, using different amounts of Hf^{4+}, its crystal lattice defect would become more varied than hexagonal $NaYF_4$.

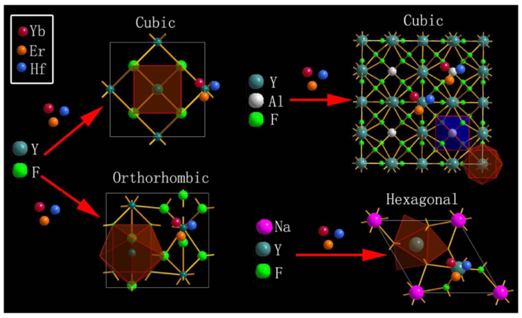

Figure 1. Schematic diagram of our theory.

2. EXPERIMENTAL SECTION

All chemicals were of analytical grade and used as received without further purification. $M(NO_3)_3$ (where M = Y, Al, Ga, In), $Ln(NO_3)_3 \cdot 6H_2O$ (where Ln = Yb, Er), HfF_4, oleic acid, sodium hydroxide (NaOH), ethanol, and hydrofluoric acid (HF) (40 wt %) were all supplied by Sinopharm Chemical Reagent Company. Deionized (DI) water was used throughout the washing process.

2.1. Synthesis of Cubic $Y_{3.2}M_{0.32}Yb_{0.4}Er_{0.08}F_{12}$ Nanoparticles. In a typical procedure to prepare cubic $Y_{3.2}M_{0.32}Yb_{0.4}Er_{0.08}F_{12}$ nanoparticles, stoichiometric amounts of $M(NO_3)_3$ and $Ln(NO_3)_3 \cdot 6H_2O$ (0.5 mol/L) precursor aqueous solutions were mixed with oleic acid (20 mL) under thorough stirring, and then 5 mL of HF solution (1.0 mol/L) was added dropwise to the mixture and the pH value was adjusted to 3.0 by using ammonia−water. After vigorous stirring at room temperature for 30 min, the resulting solution was transferred into an 80-mL Teflon-lined autoclave, sealed and heated at 170 °C for

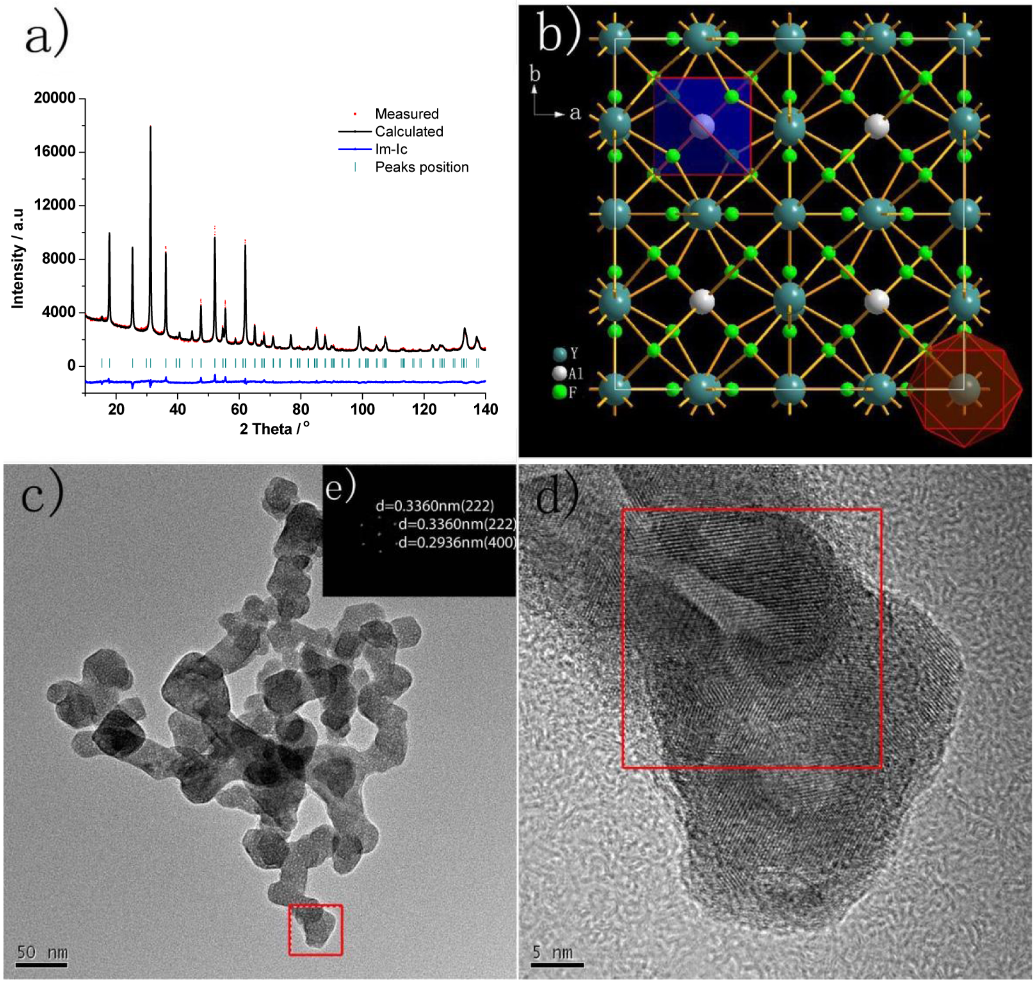

Figure 2. (a) Crystal structure refinement result pattern, (b) crystal structure diagram, (c) transmission electron microscopy (TEM) photomicrograph, and (d) high-resolution transmission electron microscopy (HRTEM) photomicrograph of $Y_{3.2}Al_{0.32}Yb_{0.4}Er_{0.08}F_{12}$. Inset (e) shows the Fourier transform of the red square area noted in panels (c) and (d).

DOI: 10.1021/ic5027976
Inorg. Chem. 2015, 54, 2643−2651

Table 1. Atomic Parameters of $Y_{3.2}Al_{0.32}Yb_{0.4}Er_{0.08}F_{12}$

name	*X* (sx)	*Y* (sy)	*Z* (sz)	*B* (sB)	Occ. (sOcc.)	Wyckoff
Y1	0.2412(3)	0.00000	0.00000	0.6334(5)	0.9696	24e
Yb1	0.2412(3)	0.00000	0.00000	0.6334(5)	0.1086	24e
Er1	0.2412(3)	0.00000	0.00000	0.6334(5)	0.0217	24e
Al1	0.25000	0.25000	0.25000	0.6254(3)	0.2667	8c
Y2	0.25000	0.25000	0.25000	0.6254(3)	0.0667	8c
F1	0.1128(3)	0.1128(3)	0.1128(3)	0.6320	1.0000	32f
F2	0.50000	0.16776(21)	0.16776(21)	0.7251	1.0000	48i

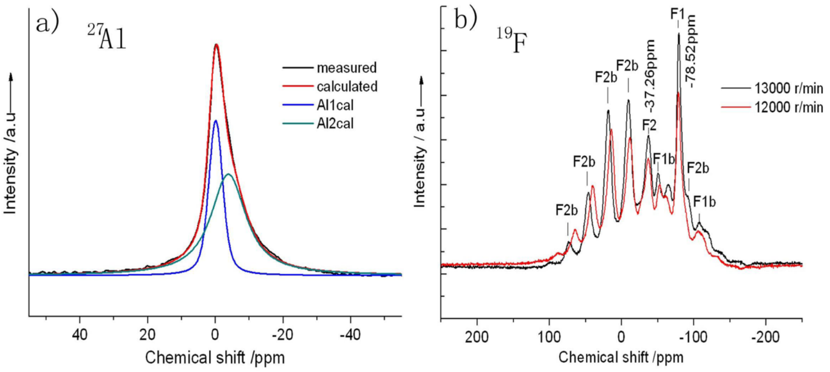

Figure 3. (a) ^{27}Al NMR spectra of sample Al. (b) ^{19}F NMR spectrum with different spin speeds of the Al sample.

12 h. The final products were collected by centrifugation, and then washed with cyclohexane and ethanol several times. The Hf^{4+}-doped $Y_{3.2}M_{0.32}Yb_{0.4}Er_{0.08}F_{12}$ was prepared by adding HfF_4 solution with designed stoichiometric amounts (0, 2, 4, 6, 8 mol %) to the reaction system. And named samples as M and Hf*x* (doping concentration percentage value), respectively. In this research work, the concentration of Er^{3+} and Yb^{3+} ions was fixed to be 2 mol % and 10 mol % for all samples, respectively.

2.2. Synthesis of Hexagonal $NaY_{0.88}Yb_{0.10}Er_{0.02}F_4$ Nanoparticles. In a typical procedure, a stoichiometric amount of $Y(NO_3)_3$ and $Ln(NO_3)_3{\cdot}6H_2O$ (0.5 mol/L) were mixed with 10 mL NaOH (1 mol/L) and oleic acid (20 mL) under thorough stirring. Then, 5 mL of HF solution (1.0 mol/L) was added dropwise to the mixture and the pH value was adjusted to 3.0 with NaOH (1 mol/L). After vigorous stirring at room temperature for ~30 min, the solution were transferred to an 80-mL Teflon-lined autoclave, sealed and heated at 190 °C for 12 h. The final products were collected, washed several times with cyclohexane and ethanol alternately. The Hf^{4+}-doped $NaY_{0.88}Yb_{0.10}Er_{0.02}F_4$ was prepared by adding HfF_4 solution with designed stoichiometric amounts (0, 2, 4, 6, 8 mol %) to the reaction system, and named samples as Hf*x* (where *x* represents the doping concentration percentage value), respectively.

2.3. Characterizations. Element composition of the as-synthesized samples were analyzed by ICP Ultima2 (Jobin Yvon). Crystalline structure was characterized by powder X-ray diffraction (XRD) method by using a Panalytical X'pert Pro MPD powder diffractometer at a scanning rate of 1°/min in the 2θ range of 10°−120°, using Co Kα radiation (λ = 0.178901 nm) and Fe filter. The morphologies, sizes, high-resolution transmission electron microscopy (TEM) images, electron energy-dispersive spectroscopy (EDS), and high-angle angular dark-field scan transmission electron microscopy (HAADF-STEM) elemental distribution mapping of samples were observed by a FEI Tecnai G2 F20 S-TWIN TEM system with a field-emission gun operated at 200 kV. Nuclear magnetic resonance (NMR) experiments of ^{9}F and ^{27}Al were carried out with an NMR spectrometer (Bruker Model AVANCE III 500), at Larmor frequencies of 470.44 and 130.28 MHz, respectively, using 4-mm Bruker MAS probes. One-dimensional ^{19}F and ^{27}Al MAS NMR spectra were recorded by using a single-pulse experiment with a typical pulse width of ~1 μs, and the rotating speed of the rotator is 12 or 13 kHz. The UC emission spectra were recorded via a fluorescence spectrophotometry (FS) system (Edinburgh Instruments, Model FSP920-C) that was equipped with a 980-nm laser (OPTEK OPO) and an integrating sphere. UC emission spectrum of samples was measured with 980-nm Q-switch pulsed OPO laser excitation. The parameters of the excitation laser were as follows: pulse width, 5 ns; repeat frequency, 10 Hz; and precise power density, 5 W/cm^2. All samples were measured under the same conditions. X-ray photoelectron spectra (XPS) were recorded with an America Thermo Scientific ESCALAB 250 system. All measurements were carried out with the same parameters at room temperature.

3. RESULTS AND DISCUSSION

3.1. Crystal Structure of $Y_{3.2}M_{0.32}Yb_{0.4}Er_{0.08}F_{12}$. Element composition and crystalline structure of different M ion co-doping samples were analyzed using inductively coupled plasma (ICP) and an XRD goniometer, respectively. Elemental quantitative results are coherent with designed stoichiometric amounts (see Table S1 in the Supporting Information). XRD peaks (Figure S1 in the Supporting Information) are similar and cannot correspond to the cubic phase of YF_3 (JCPDS File Card No. 72-0579) and the orthogonal phase of YF_3 (JCPDS File Card No. 70-1935) phases of YF_3. Furthermore, it cannot be indexed to any other phases in the JCPDS database (2008 version) and Internet reports, which implies that it should be a new phase. To further understand the exact structure of the phase, software Expo2013 and Fullprof were used to solve and refine the crystal structures of the Al sample, respectively, as shown in Figure 2. The refinement agreement indexes are R_p = 3.49%, R_{wp} = 4.87%, R_{exp} = 3.00%, and goodness of fit (GOF) = 1.65, which implies that the refinement results are credible. Crystal structural data are shown in Table 1. Y^{3+} and Al^{3+} ions located at 24e and 8c Wyckoff positions with 8-fold and 4-fold to F^-, respectively. The morphologies, sizes, and high-resolution crystalline lattice fringes were analyzed by means of TEM analysis. As shown by Figures 2d and 2e shown, the lattice fringes at *d* values of 0.3360 and 0.2936 nm can be indexed to the (222) and (400) lattice planes of the cubic phase, with *a* = 1.154 nm and space group $Fm\bar{3}m$, respectively,

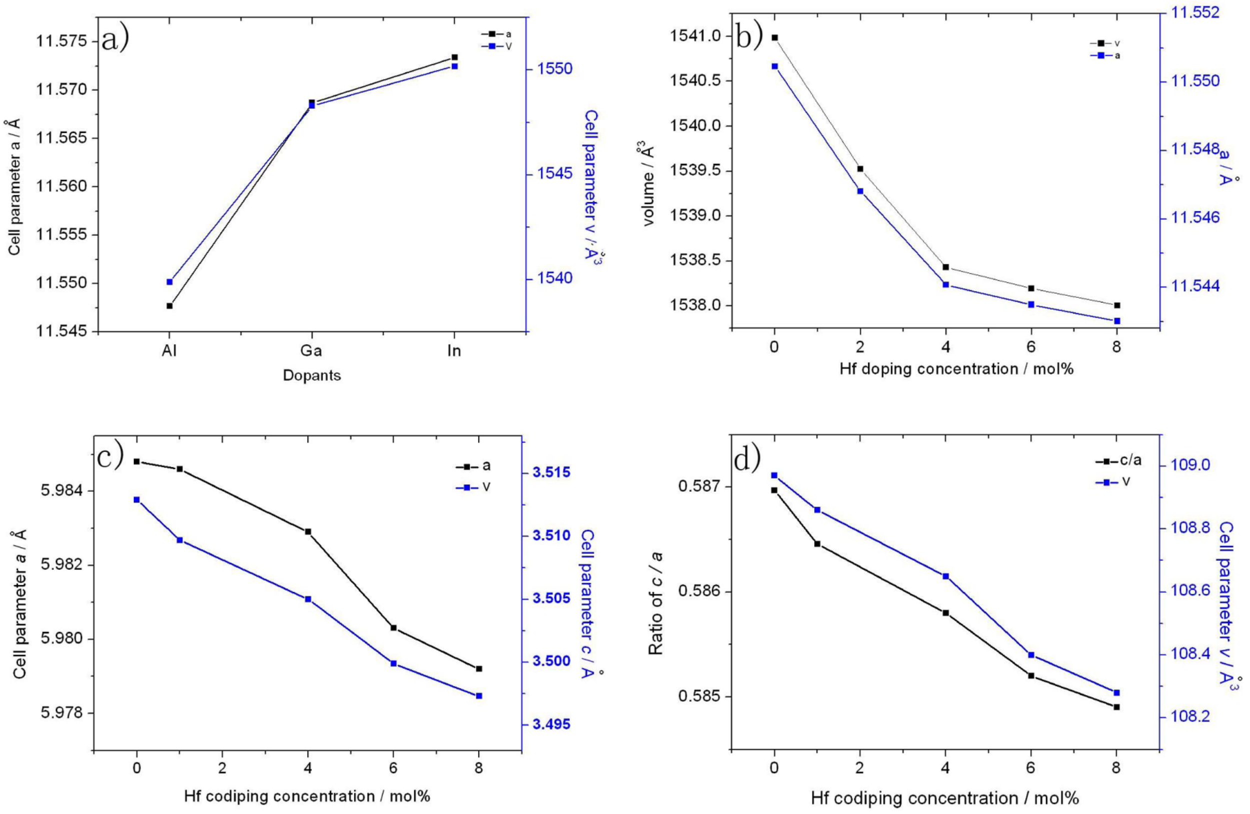

Figure 4. Changing trends in (a) cell parameter of Al, Ga, In samples and (b) different Hf^{4+} concentrations for co-doping $Y_{3.2}Al_{0.32}Yb_{0.4}Er_{0.08}F_{12}$ samples. Changing trends in cell volume ((c) cell parameters *a* and *c* and (d) ratio of *c*/*a*) for different Hf^{4+} co-doping concentrations in $NaY_{0.88}Yb_{0.10}Er_{0.02}F_4$ samples.

which agree well with the XRD analysis results. Crystal grain size is ~45 nm. The EDS analysis result is also consistent with ICP (see Figure S2 in the Supporting Information) and experimental design. NMR analysis was carried out to check the coordination environment of Al^{3+} and F^- ions. Figure 3a shows two peaks of the ^{27}Al NMR spectrum, which revealed that Al^{3+} were located at two different sites with different coordination environments, implying that some Al^{3+} ions were located at Y^{3+} positions while some Y^{3+} ions were located at Al^{3+} sites as an interchange. As an inference, the similar radius co-doping ions (Yb^{3+}/Er^{3+}) would be synchronously located at the Al^{3+} and Y^{3+} site. As shown in Figure 3b, two peaks of the ^{19}F NMR spectrum (−37.26 ppm and −78.52 ppm) were not shifted under different rotator spin speeds (12000 rpm or 13000 rpm), implying that F^- ions were coordinated with two different coordination surroundings. This phenomenon matches the crystal structure characteristic of the XRD analysis results well. According to above crystal structure analysis results, the coordination environments and crystal field asymmetry of Yb^{3+}/Er^{3+} in the Al sample vary.

3.2. Upconversion Performance of $Y_{3.2}M_{0.32}Yb_{0.4}Er_{0.08}F_{12}$. Typical UC emission spectrum of Er^{3+}-doped cubic $Y_{3.2}M_{0.32}Yb_{0.4}Er_{0.08}F_{12}$ (M = Al, Ga, In) are shown in Figure S3 in the Supporting Information. The interesting point is that the UC emission intensities of $Y_{3.2}M_{0.32}Yb_{0.4}Er_{0.08}F_{12}$ become weaker as the M radii get larger (53.5 pm for Al^{3+}, 62 pm for Ga^{3+}, 80 pm for In^{3+}). Their crystalline grain sizes are similar (40−60 nm; see Figure S4 in the Supporting Information), so the size effect on luminescence intensity can be ignored. According to the crystalline structure characteristic of cubic $Y_{3.2}M_{0.32}Yb_{0.4}Er_{0.08}F_{12}$, the crystal field asymmetry and coordination surrounding the distortion of Er^{3+}/Yb^{3+} are reduced as the M radii increases, because the radius of M is closer to that of Y^{3+}/ Er^{3+}/Yb^{3+}. It can be certified by the increasing cell parameters shown in Figure 4a. The difference in radius between M and Y was reduced as the dopant radius increased. According to Judd−Ofelt theory,[25,26] the change of UC emission intensity can be attributed to the reduction of crystal field asymmetry[30,31] and coordination surrounding dissimilarity.

3.3. Crystal Structure of Hf^{4+} Co-doping Samples. In order to further certify our theory, different concentrations of Hf^{4+} were tridoped into cubic $Y_{3.2}Al_{0.32}Yb_{0.4}Er_{0.08}F_{12}$ and hexagonal $NaY_{0.88}Yb_{0.1}Er_{0.02}F_4$, and the doping concentrations of $Er^{3+}$and Yb^{3+} were fixed to 2 mol % and 10 mol %, respectively. XRD analysis revealed that phase transition did not occur after different Hf^{4+} concentrations were co-doped (see Figure S5 in the Supporting Information). In addition, ICP analysis results are coincident with the experimental design concentration (see Tables S2 and S3 in the Supporting Information). It is important to note that the material under study is investigated without the addition of charge compensators; according to the charge compensation mechanism, the investigated samples pose some cationic vacancies or anionic interval occupation due to the imbalance of charges between Y^{3+} and Hf^{4+}. In order to understand the structural changes caused by different Hf^{4+} concentrations in tridoped samples, the crystal structure refinement of doping samples with different amounts of Hf^{4+} were carried out with fullprof software; the refinement results are shown in Figure S6 in the Supporting Information. All agreement indices are <6%, and GOF value ranges from 1.3 to 1.65, indicating that the Rietveld

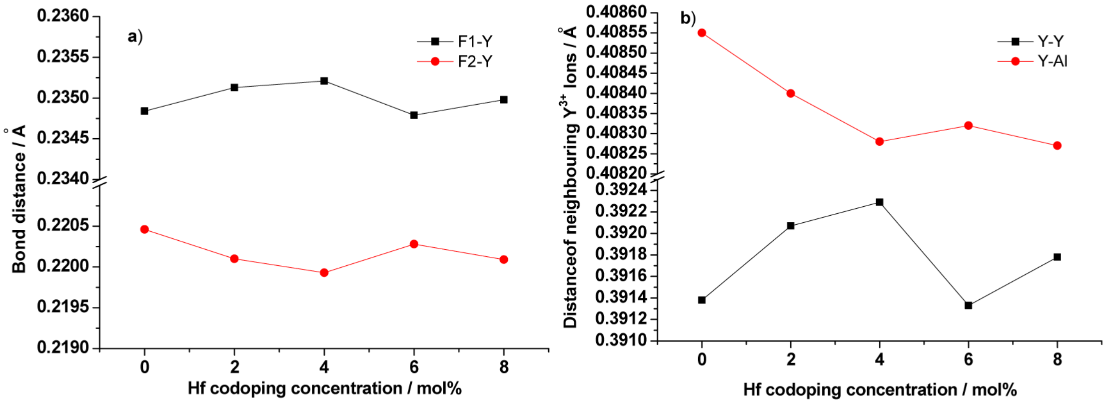

Figure 5. (a) Changes in the F1−Y and F2−Y bond distances of cubic $Y_{3.2}Al_{0.32}Yb_{0.4}Er_{0.08}F_{12}$, relative to the increasing Hf^{4+} co-doping concentration. (b) Changes in the spacing of the neighboring Y and Al ions of cubic $Y_{3.2}Al_{0.32}Yb_{0.4}Er_{0.08}F_{12}$, relative to the increasing Hf^{4+} co-doping concentration.

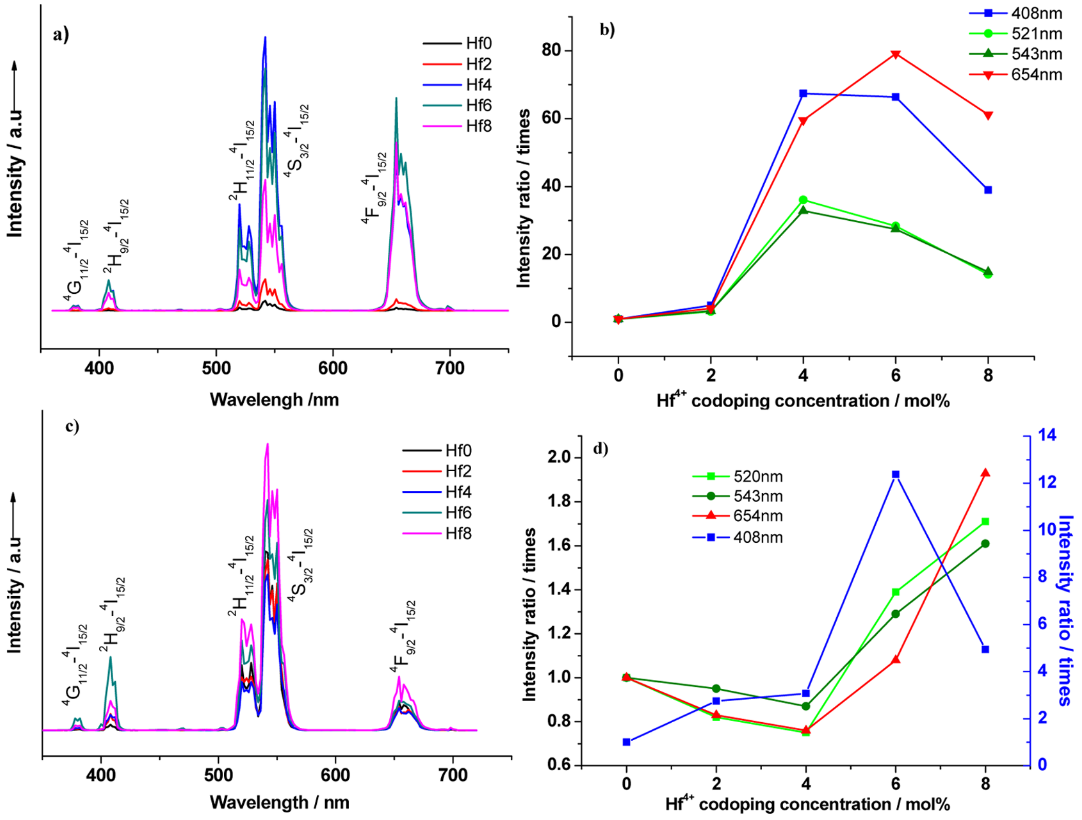

Figure 6. Changing trends in (a) upconversion spectra and (b) emission intensity of co-doping different Hf^{4+} concentrations in cubic $Y_{3.2}Al_{0.32}Yb_{0.4}Er_{0.08}F_{12}$. Changing trends in (c) upconversion spectra and (b) emission intensity of co-doping different Hf^{4+} concentrations in hexagonal $NaY_{0.88}Yb_{0.1}Er_{0.02}F_4$.

refinement is credible. Results demonstrate that their cell parameters decreased as the Hf^{4+} doping concentration increased, as shown in Figures 4b–d, implying that Hf^{4+} was doped into the crystal lattice, since the radius of the Hf ion (71 pm) is smaller than that of the Y ion (90 pm). Figure 5a shows the difference in the F1−Y and F2−Y bond distances of cubic $Y_{3.2}Al_{0.32}Yb_{0.4}Er_{0.08}F_{12}$; the graph indicates that the differences were expanded at first, then diminished, and reached a peak with a co-doping of 4 mol % Hf^{4+}. Figure 5b shows the changing trend in the spacing of neighboring Y^{3+} and Al^{3+} ions in cubic $Y_{3.2}Al_{0.32}Yb_{0.4}Er_{0.08}F_{12}$; this figure shows that the spacing initially decreased, reached a minimum at a co-doping of 4 mol % Hf^{4+}, and then increased as the Hf^{4+} doping concentration increased further.

3.4. Upconversion Performance of Hf^{4+} Co-doping Samples.

UC emission spectrum are shown in Figure 6. The structures and positions for all of the bands are in agreement with the results reported in the literature. These bands are assigned to the following transitions: $^4G_{11/2}$ to $^4I_{15/2}$, ~378 nm; $^2H_{9/2}$ to $^4I_{15/2}$, ~408 nm; $^2H_{11/2}$ to $^4I_{15/2}$, ~520 nm; $^4S_{3/2}$ to $^4I_{15/2}$, ~540 nm; and $^4F_{9/2}$ to $^4I_{15/2}$, ~654 nm.[1,13] It is surprising to observe that UC emission intensities were obviously enhanced as the Hf^{4+} co-doping concentration increased. The 654-nm emission was greatly enhanced, by a factor of ~80, with 6 mol % Hf^{4+} co-doping, compared to the sample without Hf^{4+}

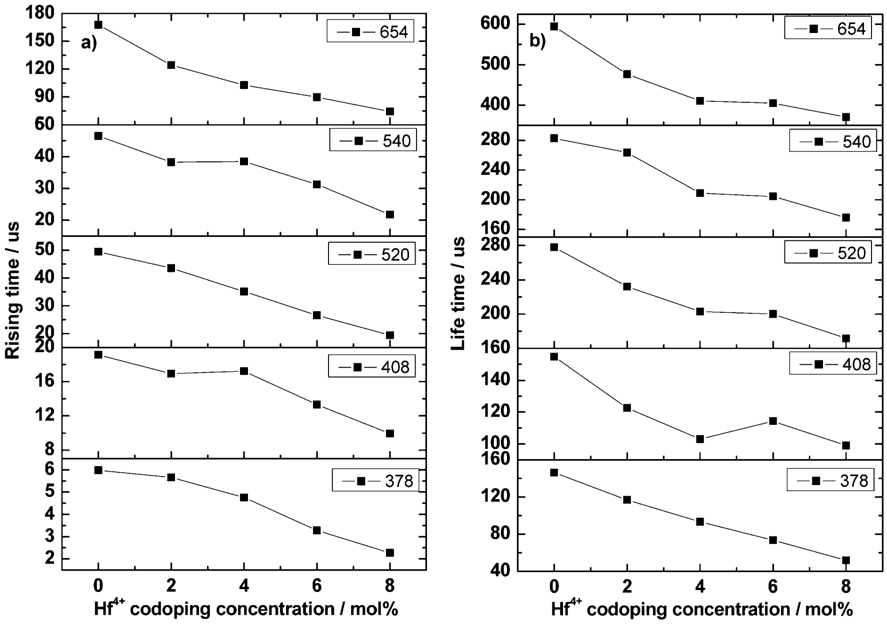

Figure 7. Changing trends in (a) rising time and (b) lifetime of different concentrations of Hf^{4+} co-doped in cubic $Y_{3.2}Al_{0.32}Yb_{0.4}Er_{0.08}F_{12}$.

doping, and the 408-nm, 521-nm, and 543-nm emissions were also enhanced, by factors of ~70, ~36, and ~32, respectively, with a co-doping of 4 mol % Hf^{4+}. Figure S7 in the Supporting Information shows that short wavelength bands for the 378-nm and 408-nm emissions were effectively enhanced with suitable co-doping amounts of Hf^{4+}. However, other UC emissions were enhanced indistinctly with the same amount of Hf^{4+} codoped in hexagonal $NaY_{0.88}Yb_{0.1}Er_{0.02}F_4$. The 521-nm, 543-nm, and 654-nm emissions were only enhanced by a factor of ~2, and the 408-nm emission was enhanced by a factor of 12 with a co-doping of 6 mol % Hf^{4+}. Rare-earth doping concentrations of all of the samples were the same, and crystal sizes were similar (~40−60 nm), as shown in Figures S8 and S9 in the Supporting Information. All emissions lifetimes of cubic phase samples were calculated using a one-exponent decay equation:[32]

$$I(t) = A - B_1 \exp\left(-\frac{t}{T_r}\right) + B_2 \exp\left(-\frac{t}{T_d}\right)$$

where T_r and T_d denote rising and decay components, respectively. Changing trends in decay time are shown in Figure 7, and the fitting results are shown in Figure S10 in the Supporting Information. All rising time constants decreased as the Hf^{4+} co-doping concentration increased, except for two singular points with a co-doping of 4 mol % Hf^{4+}.

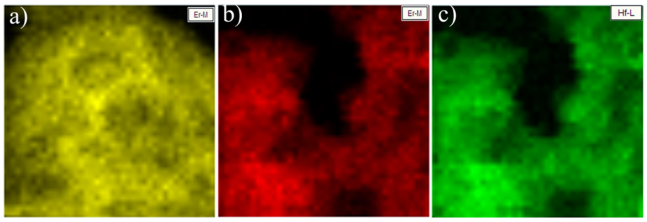

Figure 8. HAADF STEM images showing the elemental distribution for (a) Er^{3+} in sample Hf0, (b) Er^{3+} in sample Hf4, and (c) Hf^{4+} in sample Hf4.

3.5. The Upconversion (UC) Mechanism.

According to the preceding experimental results, the variation of UC luminescence properties can be attributed to the following reasons. First, samples were prepared via the hydrothermal method and the radii of Er^{3+}/Yb^{3+} and Y^{3+} ions are very close; therefore, the rare-earth ions would be distributed randomly in space, Er^{3+}/Yb^{3+} ions dispersion should be driven by the charge gradient of prodromic solution with different amounts of Hf^{4+} added in, since the charge of Hf^{4+} is higher than that of Er^{3+}/Yb^{3+}. As a result, the distribution of rare-earth ions was improved and their clusters would be reduced after co-doping with Hf^{4+}. This can be certified by HAADF STEM element distribution mapping. As shown in Figure 8, there are some high light points in Figure 8a indicating Er^{3+} clusters in sample Hf0 is obvious. However, the brightness of the pictures in Figures 8b and 8c is more uniform than that in Figure 8a, indicating that element distribution of Er^{3+} and Hf^{4+} in sample Hf4 is more uniform than in sample Hf0. Thus, the luminescence quenching among rare-earth ions would be reduced subsequently. Second, it is a common sense that crystal field asymmetry were changed synchronously with the changes in the F1−Y and F2−Y bond distances. Figure 5a reveals the *D*-value of the F1−Y and F2−Y bond distances as the Hf^{4+} codoping concentration increases, indicating that the degree of crystal field asymmetry of sample Hf4 is the largest, and changing trend are the same with bond distance. On the other hand, in order to establish charge balance that some cation vacancy or anion gap should be produced. In this case, the surroundings of Yb^{3+}/Er^{3+} are varied; as a result, the electric density was redistributed, the crystal field became misshapen, and the crystal field asymmetry was exacerbated. It can be further certified by F^- XPS analysis. Figure 9a reveals that another higher binding energy peak appeared in XPS spectra, which varied as the Hf^{4+} co-doping concentration increased, and the changing trend was synchronous with the *D*-value of the bond distance. According to Judd−Ofelt theory, the coordination environment of rare-earth ions are sensitive to luminescence emission, hypersensitive transition can be promoted effectively with increasing crystal field asymmetry. In this investigation, the $^4I_{15/2}$ to $^4G_{11/2}$ transition of Er^{3+}

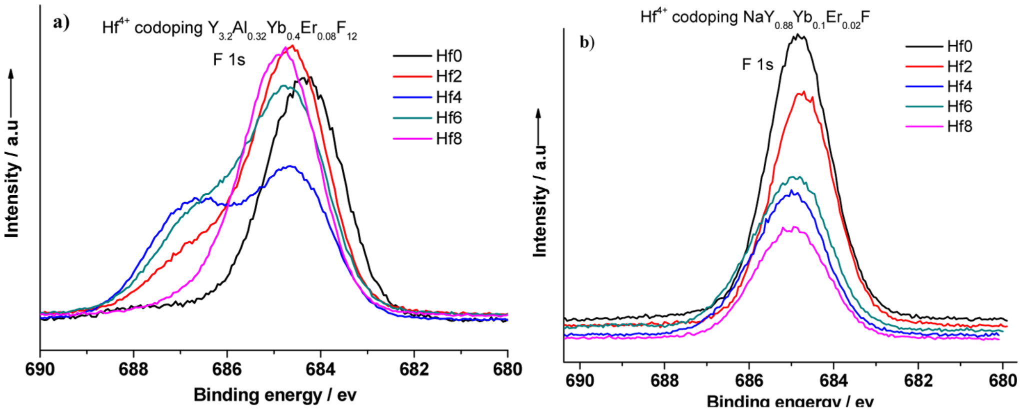

Figure 9. F^- XPS spectra of different Hf^{4+} co-doping concentrations for (a) cubic $Y_{3.2}Al_{0.32}Yb_{0.4}Er_{0.08}F_{12}$ and (b) hexagonal $NaY_{0.88}Yb_{0.1}Er_{0.02}F_4$.

(~378 nm) and the $^4I_{15/2}$ to $^2H_{11/2}$ transition of Er^{3+} (~520 nm) conform to the hypersensitive transition selection rule ($\Delta J = 2$);[33] the electron population of $^4G_{11/2}$ and $^2H_{11/2}$ level should increase as the crystal field asymmetry increases.[30,31,34] Therefore, the UC luminescence intensity were largely enhanced with a co-doping of 4 mol % Hf^{4+}. Third, the energy transition between Yb^{3+} and Er^{3+} was dependent on the interval and the variety in their coordination surroundings. Energy transition probability can be improved by shortening the interval of them, and reducing the difference of energy level gap between them. The energy level of rare-earth ions can be adjusted by improving the degree of asymmetry of the crystal field and variety of their coordination surroundings. Figure 5b shows that the interval of trivalent ions initially decreased and then increased, with a co-doping of 4 mol % Hf^{4+} as the inflection point; the changing trend was the same as that observed with UC luminescence intensity. The implied shortened interval of trivalent ions was an important reason for the enhancement in UC luminescence.

Based on the above analysis, the UC transition mechanism of $Y_{3.2}Al_{0.32}Yb_{0.4}Er_{0.08}F_{12}$ can be illustrated as shown in Figure 7f. The $^4G_{11/2}$ and $^2H_{11/2}$ levels were populated by hypersensitive transition from the ground state by multiphoton absorption or cooperation energy transition. The $^2H_{9/2}$ level was populated by electron relaxation from the upper energy level $^4G_{11/2}$, and the electron population of the $^4S_{3/2}$ energy level was populated almost from $^2H_{11/2}$ and $^2H_{9/2}$ level relaxation. The $^4F_{9/2}$ energy level was populated by electron relaxation from $^4S_{3/2}$ and other upper energy levels. Usually, the population that comes from ground-state absorption is faster than that from relaxation from higher levels, because relaxation speed relied on the lifetime of higher energy level and the populated time of the upper energy level. As Figure 10 shows, the 378-nm emission initially increased and the 654-nm emission increased in all of the samples; the 520-nm and 543-nm emission decay curves were almost concurrent and it crossed with the 408-nm emission. The cross point was initially shifted to an earlier time and then deferred as the Hf^{4+} co-doping concentration increased. In the early part of the cross point, the 520-nm emission increased faster than that at the 408-nm emission; after the cross point, the reverse is observed. By implying that the $^4G_{11/2}$ level was populated by multiphoton absorption and the $^4F_{9/2}$ level was populated from higher energy levels relaxation, the population of $^2H_{9/2}$ came from $^4G_{11/2}$ relaxation, and the population of $^2H_{11/2}$ came from multiphoton absorption population. At the $^2H_{9/2}$ and $^4G_{11/2}$ levels relaxation, initially, multiphoton absorption population of the $^2H_{11/2}$ level was predominant; after the cross point, relaxation played a dominated role. The possible reason is that a large amount of electrons were populated to $^2H_{9/2}$ and $^4G_{11/2}$ levels by hypersensitive transition for the crystal field asymmetry reaching a peak, and then relaxed to the $^2H_{11/2}$ and $^4S_{3/2}$ levels. Figure 7a shows that, for all emissions, the rising time T_r were decreasing with the Hf^{4+} co-doping concentration increased, except for two singular points (at 408 and 540 nm) at a co-doping of 4 mol % Hf^{4+}. It also indicated that the hypersensitive transition of the $^4G_{11/2}$ and $^2H_{11/2}$ levels reached a peak value and then a good amount of electrons were relaxed to the $^2H_{9/2}$ and $^4S_{3/2}$ levels, respectively; as a result, their population times were prolonged. The emissions decay rule was consistent with the UC transition mechanism of our inference. Therefore, the enhancement of UC performance can be attributed to hypersensitive transition population.

According to the above crystal structure analysis, the coordination surroundings of the rare-earth ions of cubic $Y_{3.2}Al_{0.32}Yb_{0.4}Er_{0.08}F_{12}$ (CM) were more varied and the crystal field asymmetry of CM was larger than hexagonal $NaY_{0.88}Yb_{0.1}Er_{0.02}F_4$ (HM) with the same amount of Hf^{4+} co-doped. Figure 3b shows that ^{19}F shifted anisotropically, indicating that the F^- coordination surroundings were asymmetric.[35] In CM, F1 was coordinated to one Y^{3+} and one Al^{3+}, and F2 was coordinated to three Y^{3+} and one Al^{3+}, so the F^- coordination surroundings were distorted when Hf^{4+} was co-doped and replaced Y^{3+} or Al^{3+} ions for the charge compensation. However, F^- in HM was simply coordinated with ions (Y/Yb/Er) that have very similar radii, so the F^- coordination surroundings should be experience little distortion when Hf^{4+} was co-doped and replaced Y^{3+}. This observation can be further certified by F^- XPS analysis. Figure 9a reveals that another higher binding energy peak appeared in the XPS spectra, which was varied with the Hf^{4+} co-doping concentration. The peak reached a maximum with a co-doping of 4 mol % Hf^{4+}, and then decreased with further increases in Hf^{4+} co-doping concentration. This indicates that the crystal distortion was obviously enhanced at first, reached a peak at a Hf^{4+} concentration of 4 mol %, and then reduced. The higher binding energy peak was reduced gradually as the Hf^{4+} co-doping concentration increased, which would be caused by Hf^{4+} clustering at higher co-doping concentrations, and the changing trend is consistent with the changing lattice structure and UC intensity. However, Figure 4b shows that the F^- XPS peaks only have a minor shift toward higher binding energy as the

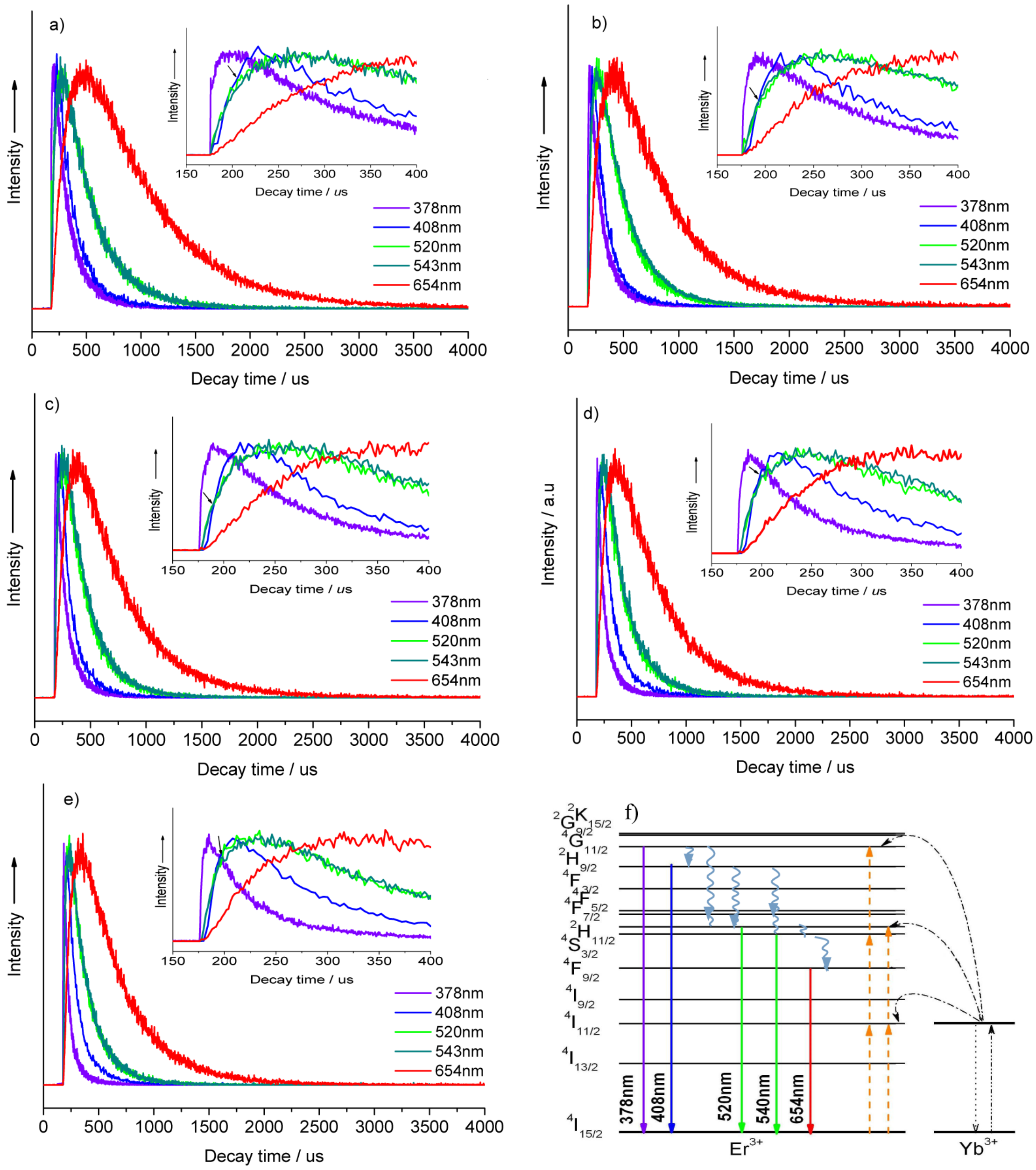

Figure 10. Decay time curves (378-nm, 408-nm, 520-nm, 543-nm, and 654-nm emissions) for various Hf^{4+} concentrations co-doped in cubic $Y_{3.2}Al_{0.32}Yb_{0.4}Er_{0.08}F_{12}$: (a) 0 mol %, (b) 2 mol %, (c) 4 mol %, (d) 6 mol %, and (e) 8 mol %. Inset illustrations show enlarged views in the range of 0–400 μs for the corresponding patterns. (f) Upconversion (UC) transition mechanism of $Y_{3.2}Al_{0.32}Yb_{0.4}Er_{0.08}F_{12}$.

Hf^{4+} co-doping concentration increases, indicating that the crystal field asymmetry was adjusted on a small scale that was smaller than CM. Thus, the coordination surroundings of the rare-earth ions in CM was more various than in HM. Crystal field asymmetry was adjusted on a larger scale with different Hf^{4+} concentrations being co-doped into CM than HM; as a result, the hypersensitive transition of $^4I_{15/2}$ to $^4G_{11/2}$ and $^4I_{15/2}$ to $^2H_{11/2}$ of CM were improved more effectively than that of HM, and UC emission intensity of CM was enhanced more obviously than HM. Distance between the adjacent rare-earth ions of CM is longer than that observed for HM, and the phonon energy of the cubic matrix may be larger than hexagonal, so the luminescence efficiency of CM is still smaller than that of HM.

4. CONCLUSION

In summary, this study has offered a new route to enhance upconversion (UC) emission performance, and a new phase—cubic $Y_{3.2}Al_{0.32}Yb_{0.4}Er_{0.08}F_{12}$, with two different coordination sites of trivalent cations—was synthesized by introducing small ions (Al^{3+}, Ga^{3+}, and In^{3+}) into the YF_3 reaction system, and the UC emissions intensity was enhanced as the co-doping ion radius decreased. The crystal lattice distortion and the various rare-earth coordination surroundings of cubic $Y_{3.2}Al_{0.32}Yb_{0.4}Er_{0.08}F_{12}$ can be adjusted effectively by co-doping different concentrations of Hf^{4+}; as a result, the UC emission intensities were enhanced by factors of 32–80, which were more effective than co-doping the same concentration of Hf^{4+} in hexagonal $NaY_{0.88}Yb_{0.1}Er_{0.02}F_4$. Cubic $Y_{3.2}Al_{0.32}Yb_{0.4}Er_{0.08}F_{12}$ co-doped with 4 mol % Hf^{4+} has potential applications in biomedical imaging, drug delivery, photodynamic therapy, and solar energy conversion. This structure-adjust strategy can be extended to discover other high-performance UC materials.

■ ASSOCIATED CONTENT

Ⓢ Supporting Information

Experimental details, Tables S1−S3, and Figures S1−S10. This material is available free of charge via the Internet at http://pubs.acs.org.

■ AUTHOR INFORMATION

Corresponding Author

*Fax: +86-591-87893206. E-mail: 21136003@qq.com.

Notes

The authors declare no competing financial interest.

■ ACKNOWLEDGMENTS

We thank Engineer Y. Lin, for NMR measurements and analysis, and Dr. Y. H. He, for XPS measurement. This work was supported by Fujian Province Natural Science Fund (No.2013J05027) and Fujian Province Education-Science Project for Middle-aged and Young Teachers (No. JA13050).

■ REFERENCES

(1) Scheps, R. *Prog. Quant. Electron.* **1996**, *20*, 271−358.

(2) Auzel, F. *Chem. Rev.* **2004**, *104*, 139−173.

(3) Chatteriee, D. K.; Rufalhah, A. J.; Zhang, Y. *Biomaterials* **2008**, *29*, 937−943.

(4) Zhou, J.; Liu, Z.; Li, F. Y. *Chem. Soc. Rev.* **2012**, *41*, 1323−1349.

(5) Wang, C.; Cheng, L.; Liu, Z. *Biomaterials* **2011**, *32*, 1110−1120.

(6) Tian, G.; Gu, Z. J.; Zhou, L. J.; Yin, W. Y.; Liu, X. X.; Yan, L.; Jin, S.; Ren, W. L.; Xing, G. M.; Li, S. J.; Zhao, Y. L. *Adv. Mater.* **2012**, *24*, 1226−1231.

(7) Bechet, D.; Couleaud, P.; Frochot, C.; Viriot, M. L.; Guillemin, F.; Barberi-Heyob, M. *Trends Biotechnol.* **2008**, *26*, 612−621.

(8) Park, Y.; Kim, H. M.; Kim, J. H.; Moon, K. C.; Yoo, B.; Lee, K. T.; Lee, N.; Choi, Y.; Park, W.; Ling, D.; Na, K.; Moon, W. K.; Choi, S. H.; Park, H. S.; Yoon, S. Y.; Suh, Y. D.; Lee, S. H.; Hyeon, T. *Adv. Mater.* **2012**, *24*, 5755−5761.

(9) Shalav, A.; Richards, B. S.; Green, M. A. *Sol. Energy Mater. Sol. Cells* **2007**, *91*, 829−842.

(10) Liang, L.; Liu, Y.; Zhao, X.-Z. *Chem. Commun.* **2013**, *49*, 3958−3960.

(11) Vetrone, F.; Naccache, R.; Zamarron, A.; de la Fuente, A. J.; Sanz-Rodriguez, F.; Maestro, L. M.; Rodriguez, E. M.; Jaque, D.; Sole, J. G.; Capobianco, J. A. *ACS Nano* **2010**, *4*, 3254−3258.

(12) Shaoshuai, Z.; Kaimo, D.; Xiantao, W.; Guicheng, J.; Changkui, D.; Yonghu, C.; Min, Y. *Opt. Commun.* **2013**, *291*, 138−42.

(13) Hehlen, M. P.; Cockroft, N. J.; Gosnell, T. R.; Bruce, A. J. *Phys. Rev. B* **1997**, *56*, 9302−9318.

(14) Kramer, K. W.; Biner, D.; Frei, G.; Gudel, H. U.; Hehlen, M. P.; Luthi, S. R. *Chem. Mater.* **2004**, *16*, 1244−1251.

(15) Wang, F.; Deng, R. R.; Wang, J.; Wang, Q. X.; Han, Y.; Zhu, H. M.; Chen, X. Y.; Liu, X. G. *Nat. Mater.* **2011**, *10*, 968−973.

(16) Ghosh, P.; Oliva, J.; De la Rosa, E.; Haldar, K. K.; Solis, D.; Patra, A. *J. Phys. Chem. C* **2008**, *112*, 9650−9658.

(17) Xu, W.; Xu, S.; Zhu, Y.; Liu, T.; Bai, X.; Dong, B.; Xu, L.; Song, H. *Nanoscale* **2012**, *4*, 6971−6973.

(18) Feng, W.; Sun, L. D.; Yan, C. H. *Chem. Commun.* **2009**, 4393−4395.

(19) Stouwdam, J. W.; van Veggel, F. *Langmuir* **2004**, *20*, 11763−11771.

(20) Zhao, J.; Jin, D.; Schartner, E. P.; Lu, Y.; Liu, Y.; Zvyagin, A. V.; Zhang, L.; Dawes, J. M.; Xi, P.; Piper, J. A.; Goldys, E. M.; Monro, T. M. *Nat. Nanotechnol.* **2013**, *8*, 729−734.

(21) Zhang, W. H.; Ding, F.; Chou, S. Y. *Adv. Mater.* **2012**, *24*, OP236−OP241.

(22) Wang, J.; Deng, R.; MacDonald, M. A.; Chen, B.; Yuan, J.; Wang, F.; Chi, D.; Hor, T. S. A.; Zhang, P.; Liu, G.; Han, Y.; Liu, X. *Nat. Mater.* **2014**, *13*, 157−162.

(23) Chen, D.; Yu, Y.; Huang, F.; Huang, P.; Yang, A.; Wang, Y. *J. Am. Chem. Soc.* **2010**, *132*, 9976−9978.

(24) Wang, H.; Lei, M.-K. *J. Inorg. Mater.* **2006**, *21*, 803−808.

(25) Judd, B. R. *Phys. Rev.* **1962**, *127*, 750−61.

(26) Ofelt, G. S. *J. Chem. Phys.* **1962**, *37*, 511−20.

(27) Huang, Q.; Yu, J.; Ma, E.; Lin, K. *J. Phys. Chem. C* **2010**, *114*, 4719−4724.

(28) Yu, H.; Cao, W.; Huang, Q.; Ma, E.; Zhang, X.; Yu, J. *J. Solid-State Chem.* **2013**, *207*, 170−177.

(29) Yu, H.; Yu, J. *J. Lumin.* **2013**, *137*, 274−281.

(30) Bai, Y. F.; Wang, Y. X.; Yang, K.; Zhang, X. R.; Peng, G. Y.; Song, Y. L.; Pan, Z. Y.; Wang, C. H. *J. Phys. Chem. C* **2008**, *112*, 12259−12263.

(31) Cheng, Q.; Sui, J. H.; Cai, W. *Nanoscale* **2012**, *4*, 779−784.

(32) Fisher, B. R.; Eisler, H. J.; Stott, N. E.; Bawendi, M. G. *J. Phys. Chem. B* **2004**, *108*, 143−148.

(33) Richardson, F. S. *Inorg. Chem.* **1980**, *19*, 2806−2812.

(34) Reid, M. F.; Richardson, F. S. *J. Phys. Chem.* **1984**, *88*, 3579−3586.

(35) Stoeger, B.; Weil, M.; Skibsted, J. *Dalton Trans.* **2013**, *42*, 11672−11682.